

Rapid transcrustal magma movement under Iceland

Euan J. F. Mutch^{1*}, John MacLennan^{1*}, Oliver Shorttle^{1,2}, Marie Edmonds¹ and John F. Rudge^{1,3}

Magma supply from the lower crust is often proposed as a trigger mechanism for volcanic eruptions. The timescales over which magma can be transported from the deepest parts of volcanic systems are, however, poorly constrained. This uncertainty poses problems for the construction of physical models and for assessment of volcanic hazards. Here, we combined geothermobarometry with Bayesian inversion diffusion chronometry on primitive olivine crystals from the Borgarhraun eruption, northern Iceland. We find that magma took about 10 days to ascend from near-Moho storage at 24 km depth before its eruption, and therefore present timescales for transcrustal magma transport on the global spreading ridge system. Our results reveal a rapid connection between the lower and upper crust with melt transport rates of 0.02 to 0.1 m s⁻¹, which are consistent with the propagation rates observed in seismic swarms in the Icelandic lower crust. Monitoring of such events using surface CO₂ fluxes may provide one of the earliest indicators that an eruption is imminent. At the high transport rates and low CO₂ contents estimated for the Borgarhraun eruption, any effect of rising magma on surface CO₂ fluxes is limited to a period of less than two days before eruption.

There is growing evidence to suggest that active volcanic regions are fed by widespread magmatic systems that extend from the base of the crust to the surface¹. In mafic systems such as Iceland, Hawai'i and the mid-ocean ridges, crystallization of melts has been shown to occur in stacked sill-like bodies over a range of depths². Establishing the timescales of the magmatic processes operating in such systems is a major focus of volcanic petrology. Diffusion chronometry has developed into a vital tool for resolving the timescales of volcanic processes. This method involves modelling the diffusive relaxation of compositional boundaries within zoned crystals at magmatic temperatures, and has been particularly important in capturing the final stages of magma assembly before eruptions. A number of studies of shallow mafic systems have established that the timescale between magma recharge and eruption can be short, often occurring days before an eruption^{3–8}. In contrast, little is known about how rapidly melt can move through the lower crust.

Rapid transport rates (0.1–10 m s⁻¹) from the mantle have been reported for exotic magma types such as kimberlites⁹ and alkali basalts^{10,11} that are derived from low-degree, volatile-rich partial melts. However, ascent timescales of the tholeiitic and calc-alkaline magmas that feed most of the Earth's active volcanism remain poorly constrained. Moho-to-surface transport rates at one volcanic arc have been estimated to be 0.0005–0.001 m s⁻¹ by Ruprecht and Plank¹², who used a thermal model to argue for deep crystallization of forsteritic olivine. Here, we establish pre-eruptive transport times for magma that shows compelling geobarometric evidence that it was once stored close to the Moho. We use a Bayesian approach to robustly characterize uncertainties in the diffusion chronometry and to concurrently fit multi-element profiles in olivine crystals.

Borgarhraun is an early postglacial (10.5–7 kyr BP) primitive basaltic lava flow located in the Northern Volcanic Zone in northern Iceland. It displays strong petrologic evidence that it was sourced from primary magmas that resided close to the Moho (at approximately 20 km depth¹³, see Fig. 1), and thus provides direct

insight into lower crustal processes. It contains a primitive crystal cargo of magnesian olivine (Fo_{87–92}), clinopyroxene (Mg# of 0.87–0.92), Cr-spinel (Cr# of 0.25–0.42) and plagioclase (An_{80–90}) that was initially in equilibrium with a suite of diverse mantle melts¹⁴. This is shown in the diversity of the trace element composition of olivine-hosted melt inclusions¹⁴. Independent geobarometry using clinopyroxene–liquid equilibria^{15,16} and the position of the olivine–plagioclase–augite–melt saturation boundary (OPAM)¹⁷ indicate that crystallization took place at approximately 24 km depth (Fig. 1). Ultramafic cumulate nodules from Borgarhraun often show rounded crystals of olivine surrounded by clinopyroxene in a poikilitic arrangement (Fig. 2). This texture suggests that clinopyroxene replaced plagioclase as the third liquidus phase; a phenomenon observed experimentally at pressures greater than 0.6 GPa (refs. ^{18,19}). Strong correlations between CO₂ and incompatible trace elements in olivine-hosted melt inclusions also suggest that crystallization took place at depths below which CO₂ exsolves into a vapour phase²⁰.

Timescales of pre-eruptive magma mixing and transport

Individual and wehrlite olivine crystals were picked from clean, glassy tephra present in the Borgarhraun eruption crater. These olivines are normally zoned in forsterite content (X_{Fo}), Ni and Mn with rims in contact with the matrix glass (Fig. 2). The rims grew in response to the crystal mush being disaggregated, entrained into a carrier liquid (that is, melt) at depth and subsequently transported to the surface²¹.

Diffusion chronometry can be used to estimate the timescale of these processes. Current obstacles in extracting robust magmatic timescales include selecting appropriate initial conditions and deconvolving the effects of crystal growth and diffusion^{22,23}. Here we use aluminium, a slow-diffusing element in olivine that has been shown to be immobile over the timescales of interest^{24,25}, to identify the compositional control of crystal growth, and as a proxy for initial conditions. Of the 20 crystals in which Al was measured, we

¹Department of Earth Sciences, University of Cambridge, Cambridge, UK. ²Institute of Astronomy, University of Cambridge, Cambridge, UK. ³Bullard Laboratories, Department of Earth Sciences, University of Cambridge, Cambridge, UK. *e-mail: ejfm2@cam.ac.uk; jcm1004@cam.ac.uk

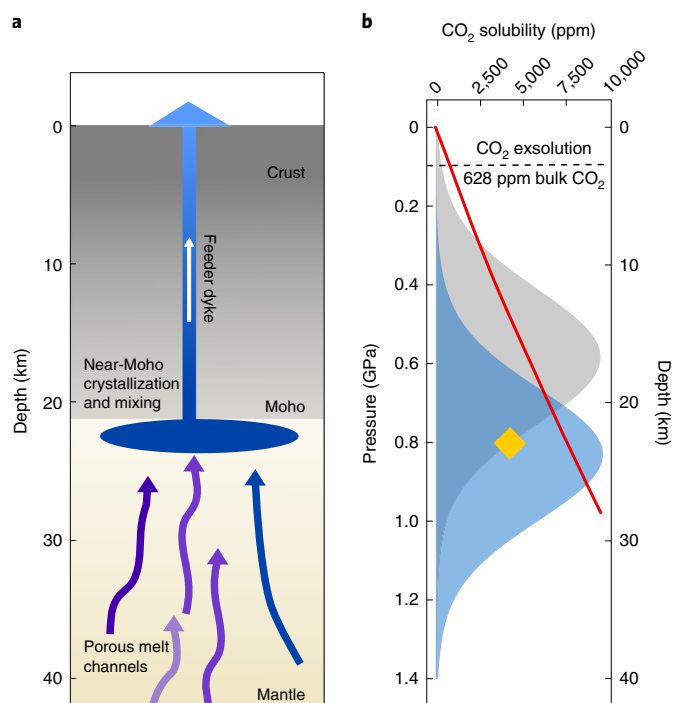


Fig. 1 | Crystallization of near-Moho magmas underneath the Theistareykir volcanic system. **a**, Schematic cross-section below northern Iceland showing the petrological model for the formation of the Borgarhraun magma (not to scale). Primary magmas leave the melting column and pool at the Moho before being transported to the surface for eruption. **b**, Storage depth estimates of the Borgarhraun magma. Pressure estimates for different clinopyroxene–liquid pairs are shown in the kernel density estimate (KDE) distributions that have been smoothed with a bandwidth of 0.14 GPa. The blue KDE corresponds to pressure estimates made by Winpenny and MacLennan¹⁵, and the grey KDE shows pressure estimates by Neave and Putirka¹⁶. The yellow diamond shows the pressure estimate made by the OPAM barometer¹⁷. The CO₂ solubility curve calculated for the Borgarhraun tephra glass composition⁴⁹ is shown by the red line. The black dashed line shows the point at which CO₂ from the Borgarhraun magma exsolves into a fluid phase.

identified two distinct populations. In the first population, there is prominent decoupling between X_{Fe} and Al ($n = 13$ crystals), which indicates control by both growth and diffusion (Supplementary Fig. 2). We will refer to this population as Al-decoupled. In the second population, Al linearly correlates with X_{Fe} across the crystal rim ($n = 7$ crystals), which indicates dominantly growth-controlled zonation (Supplementary Fig. 3). This population will be referred to as growth-dominated.

We have developed a finite element model for the one-dimensional diffusion of multiple elements in olivine (Fe–Mg, Ni, Mn) using FEniCS²⁶, and have combined this with a nested sampling Bayesian inversion²⁷ (see Methods) to estimate the timescale of crystal entrainment into the carrier liquid and transport to the surface. Al contents were converted into initial conditions for X_{Fe} , Ni and Mn assuming a linear relationship between Al and each element during olivine fractionation, and using a linear working curve between core and rim compositions. In all cases, a rim Al content of 250–260 ppm was used (see Methods). This meant that the shapes of Al profiles were mapped into X_{Fe} , Ni and Mn space, and were then used as initial conditions (now referred to as Al-based conditions). In X_{Fe} , Ni and Mn versus Al space these initial conditions appeared as straight lines (see Supplementary Figs. 2–23). Temperature (T),

pressure (P) and ferric iron content of the melt ($\text{Fe}^{3+}/\text{Fe}_{\text{total}}$) were assigned Gaussian prior distributions in the modelling, with 1σ error estimates of $1,230 \pm 30$ ²⁸, 0.8 ± 0.14 GPa^{15,17} and 0.14 ± 0.02 ²⁹. To ensure correct error propagation, we re-examined the covariance in error structure for multivariate linear fits of published experimental diffusion data^{24,30–36}, commonly parameters in the diffusion coefficients have been treated as independent. Combining this uncertainty structure with the uncertainties in the intensive parameters (P , T and oxygen fugacity (f_{O_2})) in the Bayesian inversion allows for more robust timescale uncertainty estimates, and the simultaneous consideration of all measured elemental observations.

The inversion typically converged on short magma transport timescales using Al-based initial conditions. A median timescale of 12.6 d was estimated for all modelled crystals (defined as global median), and 95% of the retrieved timescales were shorter than 37.5 d (Fig. 3). The growth-dominated crystal profiles returned median times of 7.2 d and the Al-decoupled crystals with median timescales of 16.4 d. The shortest growth-dominated crystals return times of 1.5–5 d. If growth is not considered and the crystal profiles are modelled using constant initial conditions, then the inversion calculates much longer timescales with a much wider range (global median of 24.6 d and 95% quantile of 73.5 d). This emphasizes the importance of detailed screening of crystal chemical profiles.

Determination of transcrustal magma ascent rates

The diffusion timescales recorded by the growth-dominated and Al-decoupled subpopulations should both represent mush entrainment and transport. The range in median timescale estimates (7.2–16.4 d) ultimately falls within the uncertainties of the method (see Supplementary Table 5 for uncertainties), but could also be reconciled by sectioning and anisotropy effects³⁷ or by considering incremental break-up and entrainment of the mush nodules into the carrier liquid⁷. As Borgarhraun was a pre-historic eruption, there are no records of eruption duration; however, it is expected to be similar to modern basaltic fissure eruptions which can typically last between months and years (for example the 2014–2015 Holuhraun eruption³⁸). The tephra collected as part of this study was one of the last products of the eruption, hence a feeder dyke had already been established with magma being continuously extracted. One possible interpretation is that the longer timescales of the decoupled crystals may have been caused by earlier entrainment into the carrier liquid with a longer residence time at high temperature, whereas the growth-dominated timescales represent later entrainment with rapid transport to the surface following soon after. If this were the case, then it could be speculated that the shorter timescales (1.5–5 d) represent the final transport time. The low dispersion in crystal residence times from Borgarhraun is consistent with the contention that basaltic fissure eruptions are efficient at extracting their crystal load, as is inferred for the 1783–1784 Laki fissure eruption⁷.

The OPAM barometer, which is based on rim-equilibria (Fig. 1), suggests that rim crystallization took place close to the Moho¹⁷. This would mean that the diffusion timescales represent more realistic maximum Moho-to-surface transport times than studies that do not constrain rim crystallization depth (for example ref. 12). A significant change in the major element chemistry of the melt associated with shallow crystallization would shift the OPAM estimate to lower pressures and would produce a large fraction of small crystals in the glass, which is not observed. Rapid ascent rates are needed for OPAM to preserve near-Moho pressure estimates. Near-adiabatic conditions associated with rapid magma ascent would preclude significant shallow crystallization given that the olivine saturation curve is subparallel to the adiabat and that any cooling would be minimized by efficient dyke transport¹². Rim crystallization was likely to have been associated with the cooling of the resident melt in the open magma body following disaggregation of slightly cooler mushes from the chamber margins.

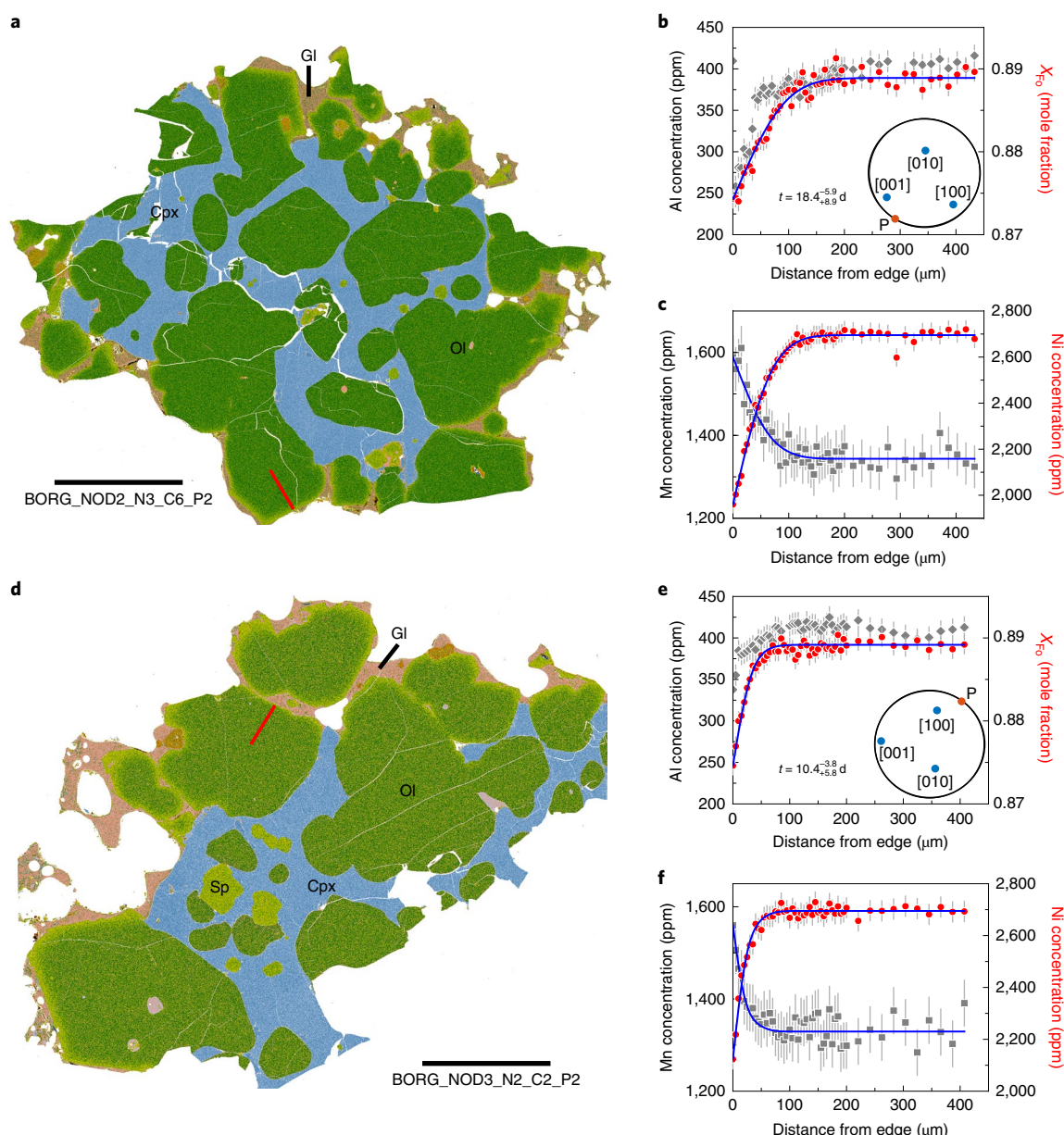


Fig. 2 | Ultramafic cumulates from the lower Icelandic crust. a, d. QEMSCAN Fe maps of wehrlitic nodules from Borgarhraun that have been colour-coded by mineral: olivine (Ol, green), clinopyroxene (Cpx, blue), glass (Gl, pink) and spinel (Sp, light green). Profile positions are shown as red lines. Scale bars, 1 mm. **b, c, e, f.** Accompanying plots showing representative zonation profiles from included magnesian olivines. Al and Mn data are grey and forsterite content in mole fraction (X_{Fo}) and Ni data are in red. Blue curves show the modelled fit for the median timescale from the Bayesian inversion (t in **b** and **e**) and correspond to the maximum likelihood fit from all three elements (X_{Fo} , Ni and Mn). The insets are equal-area pole figures that show the orientation of the crystallographic axes and the measured profile (red point, marked P). **a–c.** Sample BORG_NOD2_N3_C6_P2. **d–f.** Sample BORG_NOD3_N2_C2_P2. Both are Al-decoupled crystals (see Supplementary Figs. 14 and 17 for initial conditions). The error bars correspond to an average s.d. based on counting statistics from individual electron probe analyses and repeat measurements of the San Carlos secondary standard.

We can combine our diffusion modelling timescales with the depth estimates from geobarometry (approximately 24 km) to obtain depth-averaged magma ascent rates of $0.02\text{--}0.1\text{ m s}^{-1}$. These would be considered as minimum ascent rates as some component of the diffusion time may involve crystal residence in the carrier liquid at depth following mush entrainment. Furthermore, the rate of ascent will change with depth due to the exsolution of volatiles and changes in the mechanism of magma rise³⁹. We can then compare our estimated ascent rates to those expected for the buoyant rise of magma through the crust. We calculate the Moho-to-surface travel time of the Borgarhraun magma driven by its buoyancy alone

(see Methods). Assuming a dyke half-width of 0.5 m gives an ascent speed of 3.63 m s^{-1} , which is approximately an order of magnitude greater than the fastest rates estimated by diffusion chronometry. This could either suggest an overestimation of the dyke half-width or that mixing at depth contributed to a larger portion of the residence time. To produce our diffusion-based ascent rates and maintain thermal requirements for near-adiabatic decompression, which requires ascent rates greater than 0.01 m s^{-1} (ref.¹²), a dyke half-width of $0.02\text{--}0.06\text{ m}$ would be needed. The dyke half-widths required for our fastest ascent rates using growth-dominated crystals with shorter residence times (approximately 0.1 m for 0.1 m s^{-1})

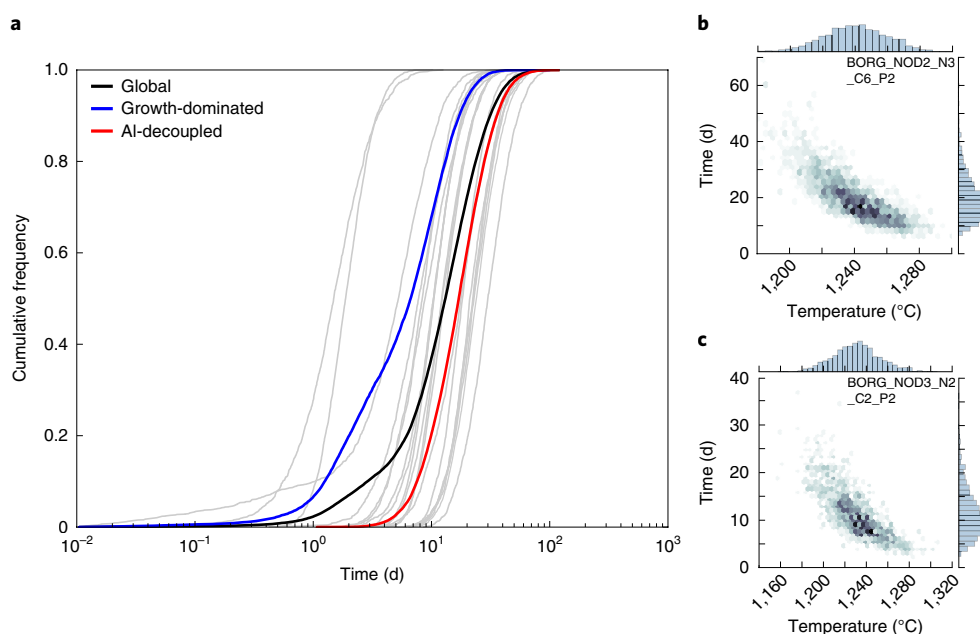


Fig. 3 | Timescales of transcrustal magma movement under the Theistareykir volcanic system. **a**, Cumulative frequency distributions showing the entrainment and transport timescale estimates from the Bayesian inversion. Grey lines are the distributions for individual modelled crystals. **b,c**, Temperature–time density plots showing the Monte Carlo realizations (posterior distribution) for profiles BORG_NOD2_N3_C6_P2 (**b**) and BORG_NOD3_N2_C2_P2 (**c**) (shown in Fig. 2). These posterior distributions are shown on the axes as blue histograms. The exponential trade-offs between temperature and time are clearly shown, given the Arrhenian relationship between diffusivity and temperature.

are similar to melt channels with 0.2–0.5 m thickness inferred from geodetic and seismic observations of mid-crustal melt propagation events^{40,41}.

Our estimated Moho-to-surface transport times are much faster than those recently made for arc basalts ($0.0005\text{--}0.001\text{ m s}^{-1}$)¹². These estimates of protracted ascent from the mantle have been attributed to temporary storage in the crust and punctuated magma transport¹². Previously, rapid ascent from the mantle was thought to be exclusively associated with exotic magmas such as nephelinites and alkali basalts ($0.1\text{--}1\text{ m s}^{-1}$)^{10,11}. We show that the parental magmas that feed many of the Earth's magmatic systems may also ascend from the mantle at high rates, albeit much lower than those estimated for volatile-rich magmas such as kimberlites ($1\text{--}10\text{ m s}^{-1}$)⁹. This emphasizes the importance of volatiles in controlling magma dynamics in addition to magma density and viscosity³⁹.

Constraints on magma transport rates from volcano seismicity

Microseismicity in the lower crust of the Icelandic magmatic systems has been linked to melt migration^{40,42–44}. In most cases, this seismicity was related to crustal accretion and the emplacement of sills in the lower crust^{40,44}. Lower crustal seismicity temporally related to eruptions at Eyjafjallajökull⁴² and Bárðarbunga⁴³ has been interpreted as melt migrating through continuous conduits linking the upper and lower crust. In the case of Eyjafjallajökull, clusters of seismic activity were detected sporadically jumping over a range of depths (12–30 km) during a two week period with melt moving aseismically between the seismic clusters⁴². Melt injection occurring in bursts propagating at $0.03\text{--}0.05\text{ m s}^{-1}$ has been inferred in the lower crust by White et al.⁴⁰. The swarms of microseismicity were documented to last for hours, punctuated by periods of quiescence lasting tens to hundreds of hours. These rates of active propagation are comparable to the ascent rates of this study. However, the stop–start nature of dyke propagation and the time periods over which deep seismicity has been detected (weeks to years) could

suggest that the timescales of initial dyke propagation may take much longer than the rate of magma transport once an open dyke is established. The process of dyke propagation could therefore be the rate-limiting step in controlling magma ascent from the lower crust.

The CO₂ outgassing flux before and during eruptions

Monitoring pre-eruptive CO₂ fluxes at the surface could prove to be a powerful tool for forecasting imminent eruptions and volcanic hazards. By combining magma ascent timescales with observational constraints on the CO₂ budget of an erupted magma, we can make exploratory models for the pre-eruptive degassing behaviour that can be detected. The texture and zoning patterns of olivine crystals from lava flows of earlier phases of the Borgarhraun eruption are similar to those observed in the tephra^{14,15,17}. The consistency in pre-eruptive residence times inferred throughout some large basaltic fissure eruptions means the ascent timescales obtained in this study could be used to approximate pre-eruptive ascent, despite being calculated from late-stage tephra⁷. The CO₂ budget of Borgarhraun is well constrained²⁰, with only the most trace-element-enriched olivine-hosted melt inclusions being close to vapour saturation. As the magma underwent minimal degassing before ascent, the bulk CO₂ content of the magma can be estimated. The rate of CO₂ outgassing at the surface can then be estimated using two endmember scenarios: open- and closed-system degassing. Pure open-system degassing assumes that CO₂ can efficiently segregate from the melt once it exsolves. In contrast, pure closed-system degassing assumes that there is no removal of CO₂ before eruption and that all degassing occurs at the vent. The temporal evolution of the eruption rate was estimated using a total eruptive volume of 0.35 km^3 (ref. 17) and an eruption decay rate and duration similar to that of Holuhraun³⁸ (see Methods). Estimated peak eruptive CO₂ fluxes of 13 kt d^{-1} for open-system degassing (inset in Fig. 4) are comparable to those measured before explosive paroxysms at Stromboli (11 kt d^{-1})⁴⁵, and those estimated for the recent Icelandic fissure eruptions Laki ($20\text{--}360\text{ kt d}^{-1}$)⁷ and Holuhraun ($50\text{--}110\text{ kt d}^{-1}$)⁴⁶. CO₂ fluxes of a similar order of

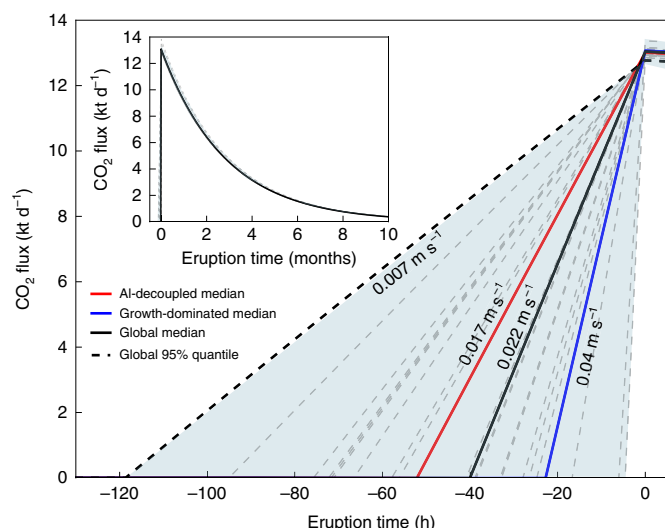


Fig. 4 | Exploratory models of open-system pre-eruptive CO₂ fluxes at Borgarhraun. The models use estimated ascent rates from diffusion timescales and estimates of eruption rate parameters from modern observations at Holuhraun. Grey dashed lines are flux estimates made using the median diffusion timescales for individual crystals, and the coloured lines correspond to flux estimates made from median timescales of modelled crystal populations. Calculated ascent velocities are shown next to the curves. The shaded region shows the range of possible fluxes based on all of the modelled crystals. Inset, the calculated CO₂ flux during the eruption, assuming an eruption duration and decay in eruption rate similar to that of Holuhraun³⁸.

magnitude (41.6 ktd⁻¹) have also been measured from space during an eruption at Yasur volcano⁴⁷. Background soil CO₂ fluxes routinely measured in volcanically active regions are typically on the order of 0.001–0.1 kt d⁻¹ (ref. ⁴⁸).

The bulk CO₂ content of the melt for Borgarhraun is 628 ppm (refs. ^{17,20}), meaning that the melt becomes saturated in a CO₂-rich vapour phase at approximately 3 km depth⁴⁹ (Fig. 1). For open-system degassing, an increase in CO₂ flux above typical background levels will be observed approximately 40 h before eruption using a median ascent timescale from the diffusion modelling results of all measured crystals (Fig. 4). Longer ascent timescales on the order estimated using Al-decoupled crystals would show elevated CO₂ fluxes approximately 50 h before eruption. Elevations in surface CO₂ fluxes would only be detected 5–20 h before eruption at the faster ascent rates of the growth-dominated crystals. These detection times would be considered maximum estimates as bubble segregation following exsolution can only take place once the yield strength of the melt is overcome. Only once the diameter of a bubble exceeds a critical threshold, through expansion and coalescence, can it rise buoyantly through a moving liquid⁵⁰. For the closed-system case, the CO₂ cannot segregate from the melt and there would be no pre-eruptive CO₂ flux. Given the rapid rates of ascent and minimal storage time in the shallow crust, it is unlikely that many CO₂ bubbles would grow large enough to segregate from the melt, meaning that any pre-eruptive CO₂ fluxes will lie between the two endmember degassing scenarios. Consequently, detecting elevated CO₂ fluxes as an eruption precursor may have limited scope to provide adequate warning for these volatile-poor magmas that ascend rapidly from great depth. It also suggests that CO₂ outgassing from these types of near-Moho magmas will mostly occur during eruption, which will have important implications for volcanic inputs to global CO₂ budgets. In ocean island settings with more enriched magma suites (such as Hawai'i), or in volcanic systems in Iceland with higher initial CO₂ levels than Borgarhraun (for example Bárðarbunga,

Eyjafjallajökull), vapour saturation occurs at higher pressure and there is a greater likelihood of elevated CO₂ fluxes before eruptions—as is observed⁵¹. Ascent velocities of these more volatile-rich magmas may be enhanced by the additional buoyancy supplied by deeper volatile exsolution³⁹.

Online content

Any methods, additional references, Nature Research reporting summaries, source data, statements of code and data availability and associated accession codes are available at <https://doi.org/10.1038/s41561-019-0376-9>.

Received: 22 April 2018; Accepted: 24 April 2019;

Published online: 24 June 2019

References

- Cashman, K. V., Sparks, R. S. J. & Blundy, J. D. Vertically extensive and unstable magmatic systems: a unified view of igneous processes. *Science* **355**, eaag3055 (2017).
- Kelemen, P. B., Koga, K. & Shimizu, N. Geochemistry of gabbro sills in the crust-mantle transition zone of the Oman ophiolite: implications for the origin of the oceanic lower crust. *Earth Planet. Sci. Lett.* **146**, 475–488 (1997).
- Costa, F. & Dungan, M. Short time scales of magmatic assimilation from diffusion modeling of multiple elements in olivine. *Geology* **33**, 837–840 (2005).
- Costa, F., Coogan, L. A. & Chakraborty, S. The time scales of magma mixing and mingling involving primitive melts and melt–mush interaction at mid-ocean ridges. *Contrib. Mineral. Petrol.* **159**, 371–387 (2010).
- Kahl, M., Chakraborty, S., Costa, F. & Pompilio, M. Dynamic plumbing system beneath volcanoes revealed by kinetic modeling, and the connection to monitoring data: an example from Mt. Etna. *Earth Planet. Sci. Lett.* **308**, 11–22 (2011).
- Rae, A. S. et al. Time scales of magma transport and mixing at Kilauea volcano, Hawai'i. *Geology* **44**, 463–466 (2016).
- Hartley, M. E., Morgan, D. J., MacLennan, J., Edmonds, M. & Thordarson, T. Tracking timescales of short-term precursors to large basaltic fissure eruptions through Fe–Mg diffusion in olivine. *Earth Planet. Sci. Lett.* **439**, 58–70 (2016).
- Pankhurst, M. J., Morgan, D. J., Thordarson, T. & Loughlin, S. C. Magmatic crystal records in time, space, and process, causatively linked with volcanic unrest. *Earth Planet. Sci. Lett.* **493**, 231–241 (2018).
- Peslier, A. H., Woodland, A. B. & Wolff, J. A. Fast kimberlite ascent rates estimated from hydrogen diffusion profiles in xenolithic mantle olivines from southern Africa. *Geochim. Cosmochim. Acta* **72**, 2711–2722 (2008).
- Demouchy, S., Jacobsen, S. D., Gaillard, F. & Stern, C. R. Rapid magma ascent recorded by water diffusion profiles in mantle olivine. *Geology* **34**, 429–432 (2006).
- Peslier, A. H., Bizimis, M. & Matney, M. Water disequilibrium in olivines from Hawaiian peridotites: recent metasomatism, H diffusion and magma ascent rates. *Geochim. Cosmochim. Acta* **154**, 98–117 (2015).
- Ruprecht, P. & Plank, T. Feeding andesitic eruptions with a high-speed connection from the mantle. *Nature* **500**, 68–72 (2013).
- Staples, R. K. et al. Faroe-Iceland Ridge Experiment 1. Crustal structure of northeastern Iceland. *J. Geophys. Res.* **102**(B4), 7849–7866 (1997).
- MacLennan, J. et al. Melt mixing and crystallization under Theistareykir, northeast Iceland. *Geochem. Geophys. Geosyst.* **4**, 8624 (2003).
- Winpenny, B. & MacLennan, J. A partial record of mixing of mantle melts preserved in Icelandic phenocrysts. *J. Petrol.* **52**, 1791–1812 (2011).
- Neave, D. A. & Putirka, K. D. A new clinopyroxene-liquid barometer, and implications for magma storage pressures under Icelandic rift zones. *Am. Mineral.* **102**, 777–794 (2017).
- MacLennan, J., McKenzie, D., Hilton, F., Gronvold, K. & Shimizu, N. Geochemical variability in a single flow from northern Iceland. *J. Geophys. Res.* **108**(B1), 2007 (2003).
- Bender, J., Hodges, F. & Bence, A. Petrogenesis of basalts from the project FAMOUS area: experimental study from 0 to 15 kbars. *Earth Planet. Sci. Lett.* **41**, 277–302 (1978).
- Weaver, J. S. & Langmuir, C. H. Calculation of phase equilibrium in mineral-melt systems. *Comput. Geosci.* **16**, 1–19 (1990).
- Hauri, E. H. et al. CO₂ content beneath northern Iceland and the variability of mantle carbon. *Geology* **46**, 55–58 (2018).
- Thomson, A. & MacLennan, J. The distribution of olivine compositions in Icelandic basalts and picrites. *J. Petrol.* **54**, 745–768 (2012).
- Dohmen, R., Faak, K. & Blundy, J. D. Chronometry and speedometry of magmatic processes using chemical diffusion in olivine, plagioclase and pyroxenes. *Rev. Mineral. Geochem.* **83**, 535–575 (2017).

23. Shea, T., Lynn, K. J. & García, M. O. Cracking the olivine zoning code: distinguishing between crystal growth and diffusion. *Geology* **43**, 935–938 (2015).
24. Spandler, C. & O'Neill, H. S. C. Diffusion and partition coefficients of minor and trace elements in San Carlos olivine at 1,300 °C with some geochemical implications. *Contrib. Mineral. Petrol.* **159**, 791–818 (2010).
25. Zhukova, I., O'Neill, H. & Campbell, I. H. A subsidiary fast-diffusing substitution mechanism of Al in forsterite investigated using diffusion experiments under controlled thermodynamic conditions. *Contrib. Mineral. Petrol.* **172**, 53 (2017).
26. Alnæs, M. et al. The FEniCS project version 1.5. *Arch. Numer. Softw.* **3**, 9–23 (2015).
27. Feroz, F., Hobson, M. & Bridges, M. MultiNest: an efficient and robust Bayesian inference tool for cosmology and particle physics. *Mon. Not. R. Astron. Soc.* **398**, 1601–1614 (2009).
28. Sugawara, T. Empirical relationships between temperature, pressure, and MgO content in olivine and pyroxene saturated liquid. *J. Geophys. Res.* **105**(B4), 8457–8472 (2000).
29. Shorttle, O. et al. Fe-XANES analyses of Reykjanes Ridge basalts: implications for oceanic crust's role in the solid Earth oxygen cycle. *Earth Planet. Sci. Lett.* **427**, 272–285 (2015).
30. Chakraborty, S. Rates and mechanisms of Fe–Mg interdiffusion in olivine at 980–1300 °C. *J. Geophys. Res.* **102**(B6), 12317–12331 (1997).
31. Petry, C., Chakraborty, S. & Palme, H. Experimental determination of Ni diffusion coefficients in olivine and their dependence on temperature, composition, oxygen fugacity, and crystallographic orientation. *Geochim. Cosmochim. Acta* **68**, 4179–4188 (2004).
32. Dohmen, R., Becker, H.-W. & Chakraborty, S. Fe–Mg diffusion in olivine I: experimental determination between 700 and 1,200 °C as a function of composition, crystal orientation and oxygen fugacity. *Phys. Chem. Miner.* **34**, 389–407 (2007).
33. Dohmen, R. & Chakraborty, S. Fe–Mg diffusion in olivine II: point defect chemistry, change of diffusion mechanisms and a model for calculation of diffusion coefficients in natural olivine. *Phys. Chem. Miner.* **34**, 409–430 (2007).
34. Holzapfel, C., Chakraborty, S., Rubie, D. & Frost, D. Effect of pressure on Fe–Mg, Ni and Mn diffusion in $(\text{Fe}_{1-x}\text{Mg}_x)_2\text{SiO}_4$ olivine. *Phys. Earth Planet. Inter.* **162**, 186–198 (2007).
35. Zhukova, I., O'Neill, H. S. C., Campbell, I. H. & Kilburn, M. R. The effect of silica activity on the diffusion of Ni and Co in olivine. *Contrib. Mineral. Petrol.* **168**, 1029 (2014).
36. Jollands, M., Hermann, J., O'Neill, H. S. C., Spandler, C. & Padrón-Navarta, J. Diffusion of Ti and some divalent cations in olivine as a function of temperature, oxygen fugacity, chemical potentials and crystal orientation. *J. Petrol.* **57**, 1983–2010 (2016).
37. Shea, T., Costa, F., Krimer, D. & Hammer, J. E. Accuracy of timescales retrieved from diffusion modeling in olivine: a 3D perspective. *Am. Mineral.* **100**, 2026–2042 (2015).
38. Gudmundsson, M. T. et al. Gradual caldera collapse at Bárðarbunga volcano, Iceland, regulated by lateral magma outflow. *Science* **353**, aaf8988 (2016).
39. Anderson, A. CO₂ and the eruptibility of picrite and komatiite. *Lithos* **34**, 19–25 (1995).
40. White, R. S. et al. Dynamics of dyke intrusion in the mid-crust of Iceland. *Earth Planet. Sci. Lett.* **304**, 300–312 (2011).
41. Hooper, A. et al. Increased capture of magma in the crust promoted by ice-cap retreat in Iceland. *Nat. Geosci.* **4**, 783–786 (2011).
42. Tarasewicz, J., Brandsdóttir, B., White, R. S., Hensch, M. & Thorbjarnardóttir, B. Using microearthquakes to track repeated magma intrusions beneath the Eyjafjallajökull stratovolcano, Iceland. *J. Geophys. Res.* **117**, B00C06 (2012).
43. Hudson, T. et al. Deep crustal melt plumbing of Bárðarbunga volcano, Iceland. *Geophys. Res. Lett.* **44**, 8785–8794 (2017).
44. Key, J., White, R. S., Soosalu, H. & Jakobsdóttir, S. S. Multiple melt injection along a spreading segment at Askja, Iceland. *Geophys. Res. Lett.* **38**, L05301 (2011).
45. Aiuppa, A. et al. Unusually large magmatic CO₂ gas emissions prior to a basaltic paroxysm. *Geophys. Res. Lett.* **37**, L17303 (2010).
46. Bali, E., Hartley, M., Halldórsson, S., Gudfinnsson, G. & Jakobsson, S. Melt inclusion constraints on volatile systematics and degassing history of the 2014–2015 Holuhraun eruption, Iceland. *Contrib. Mineral. Petrol.* **173**, 9 (2018).
47. Schwandner, F. M. et al. Spaceborne detection of localized carbon dioxide sources. *Science* **358**, eaam5782 (2017).
48. Chiodini, G., Cioni, R., Guidi, M., Raco, B. & Marini, L. Soil CO₂ flux measurements in volcanic and geothermal areas. *Appl. Geochem.* **13**, 543–552 (1998).
49. Shishkina, T., Botcharnikov, R., Holtz, F., Almeev, R. & Portnyagin, M. V. Solubility of H₂O- and CO₂-bearing fluids in tholeiitic basalts at pressures up to 500 MPa. *Chem. Geol.* **277**, 115–125 (2010).
50. Vergnolle, S. & Jaupart, C. Separated two-phase flow and basaltic eruptions. *J. Geophys. Res.* **91**(B12), 12842–12860 (1986).
51. Poland, M. P., Miklius, A., Sutton, A. J. & Thornber, C. R. A mantle-driven surge in magma supply to Kilauea Volcano during 2003–2007. *Nat. Geosci.* **5**, 295–300 (2012).

Acknowledgements

This research was funded by a NERC studentship awarded to E.J.F.M. (NE/L002507/1). We are grateful to I. Buisman and G. Lampronti for assistance with the EPMA and EBSD analyses, respectively. We would also like to thank C. Richardson for helpful advice on FEniCS.

Author contributions

The project was initially conceived by J.M. E.J.F.M. developed the diffusion model along with O.S. and J.F.R. E.J.F.M. performed the EPMA and SEM analysis, and subsequently undertook the diffusion modelling. E.J.F.M., J.M. and M.E. conducted the buoyancy and CO₂ flux modelling. E.J.F.M. wrote the first draft of the manuscript, which was revised by all authors.

Competing interests

The authors declare no competing interests.

Additional information

Supplementary information is available for this paper at <https://doi.org/10.1038/s41561-019-0376-9>.

Reprints and permissions information is available at www.nature.com/reprints.

Correspondence and requests for materials should be addressed to E.J.F.M. or J.M.

Publisher's note: Springer Nature remains neutral with regard to jurisdictional claims in published maps and institutional affiliations.

© The Author(s), under exclusive licence to Springer Nature Limited 2019

Methods

Analytical methods. Individual olivine crystals and wehrlitic nodules were separated from fresh glassy tephra collected at the Borgarhraun eruption crater (65.830°N, 16.881°W) in 2009 and 2014. These were then mounted in 1" epoxy rounds and polished using silicon carbide papers and Metprep diamond suspension down to 0.25 µm grade. The texture and zoning patterns of approximately 100 olivine crystals (both individual and wehrlitic olivines) were assessed using back-scattered electron (BSE) microscopy and energy dispersive X-ray spectroscopy (EDS) phase mapping (quantitative elemental mapping scanning; QEMSCAN) using a FEI Quanta 650FEG SEM at the University of Cambridge. BSE microscopy images were typically collected using an accelerating voltage of 10–20 kV and a working distance of 13 mm. QEMSCAN maps were collected using two Bruker XFlash 6|30 Energy Dispersive Spectrometers. The QEMSCAN system includes an automated spectrum acquisition and classification procedure. Analyses were performed by obtaining field-scans, providing a complete characterization of particle surfaces above a predefined electron back-scatter threshold. The brightness coefficients were calibrated against quartz, gold and copper. Spectra were collected at 25 kV and 10 nA with 2,000 total X-ray counts at a 2 µm spacing, and compared to a species identification protocol (SIP) that discriminates minerals on the basis of their characteristic X-ray and electron back-scatter intensities.

To minimize the influence of sectioning and multidimensional diffusive effects³⁷, crystals with large euhedral faces were selected for more in-depth analysis. Major (Mg, Fe and Si), minor (Ni, Mn, Ca and Cr) and trace element (Al) profiles were analysed by electron probe microanalysis (wavelength dispersive X-ray spectroscopy, EPMA) using a Cameca SX100 with five wavelength dispersive spectrometers at the University of Cambridge. Calibration was carried out using a mixture of natural and synthetic minerals and oxides. Instrument drift and measurement uncertainty was assessed by measuring secondary standards. An accelerating voltage of 20 kV was applied with a working current of 20 nA for major elements and 200 nA for minor and trace elements. On-peak count times of 20 s were used for major elements and 100–120 s for minor and trace elements, with half-count times off-peak. A spot size of 1 µm was selected, with profile point spacing varying from 5 µm (typically within 150 µm of the crystal edge) and 20 µm (distances exceeding 150 µm from the edge). This was to ensure both high spatial resolution and analytical precision, but also to limit analytical convolution between adjacent activation volumes. Assuming diffusion from an initial step-like function at 1,230 °C in an olivine crystal (along [100]) with $F_{0,0}$, the lower limit of 20% diffusion timescale accuracy for 5 µm spatial resolution would be approximately 0.8, 0.5 and 1 d for Fe–Mg, Ni and Mn respectively³⁵. Diffusive anisotropy in olivine was corrected for by characterizing the lattice orientations of the measured olivine crystals using electron back-scatter diffraction (EBSD). EBSD data with a resolution of 1–10 µm were collected at the University of Cambridge with a Bruker e-Flash HR EBSD detector equipped on the Quanta 650FEG SEM, operating at 20 kV, with a beam spot size of 5.5, and a stage tilt of 70°. The detector resolution was 320 pixels × 240 pixels, whereas the working distance and sample–detector distance were 17–30 mm and 12–18 mm, respectively. The data collection and indexing was performed with Bruker QUANTAX CrystAlign software³³, using a Hough transform resolution of 60–70. Data were analysed using MTEX V4.0³⁴, a freeware toolset for the commercial software package MATLAB³⁵.

Diffusion modelling. To characterize the competing influence of growth and diffusion, compositional profiles of faster-diffusing species (Mg–Fe exchange, Ni and Mn) were compared with Al (here assumed to be diffusively immobile^{24,25}) using compositional cross-plots that have been colour-coded on the basis of profile distance (for example, Supplementary Figs. 4–23). Ca and Cr were measured, but not included in the inversions. In the case of Ca, this was because secondary fluorescence from the surrounding glass influenced measurements close to the crystal edge, making it difficult to estimate appropriate boundary conditions in the diffusion model. The temporal resolution of Ca, which is a slower diffuser in olivine³⁶, is not high enough for short-timescale work, and this may introduce more uncertainty to the Bayesian inversions. For Cr, the data was too noisy to provide any useful temporal constraints. The diffusivity and anisotropy of Cr also still need to be refined in natural olivines^{37–39}.

Cross-plots that showed a strong linear correlation between Al and the element of interest for points close to the crystal edge were deemed to be growth-dominated and suggest that there was insufficient time to decouple the two elements diffusively. Crystals with cross-plots that display deviation from linearity in the rims thus show contributions from both growth and diffusion. A linear working curve between selected core and rim compositions of Al and the element of interest was subsequently used to constrain the growth-contributed initial conditions that were used in the modelling. Here we assumed that the elements of interest and Al covary linearly during olivine fractionation. The shape of selected parts of the Al profiles were thereby mapped directly into X_{Fe} , Ni and Mn space to create the Al-based initial conditions. In X_{Fe} , Ni, Mn versus Al space these initial conditions appear as a straight line (termed here the linear growth curve). Supplementary Figs. 2 and 3 show how these initial conditions were constructed and also how diffusion of the faster elements can cause distributions of X_{Fe} , Ni, and Mn versus Al to deviate from linearity. During calibration of the linear growth curve, a rim Al

content of 250–260 ppm was used in all cases, which was the lowest rim Al value observed in the Borgarhraun crystal population. These values were used to try and eliminate the effects of analytical contamination and secondary fluorescence from the adjacent glass. This was particularly important for crystals with very thin rims for which the outer rim point may not have been analysed properly (for example, Supplementary Fig. 10). In some growth-dominated crystals Ni and Al did not correlate, which we attribute to boundary layer effects on growth or complexities associated with mixing the host melt with the mush liquid⁶⁰. In such instances, Al did not form a representative initial condition, but was still incorporated into the modelling framework. These crystals produced much larger timescale uncertainties as the fit to the data was poorer.

The temperature of the carrier liquid (1,230 ± 30 °C) was estimated using the Sugawara³⁸ melt thermometer; pressure (0.8 ± 0.14 GPa) was estimated using both clinopyroxene–liquid^{15,16} and OPAM barometry^{17,61}. A Fe^{3+}/Fe_{total} value of 0.14 ± 0.02, typical of depleted Icelandic basalts²⁹, was used. Oxygen fugacity was calculated from glass compositions and Fe^{3+}/Fe_{total} using equation (7) of Kress and Carmichael⁶². The activity of SiO_2 (a_{SiO_2}) of the Borgarhraun magma (0.62 ± 0.03) was calculated using rhyolite-MELTSv1.0.2^{63,64} using the liquid's affinity for quartz of measured tephra glass compositions⁶⁵.

New multivariate regressions through a compiled database of olivine diffusion experiments^{24,30–34} were conducted for Fe–Mg exchange (Global and TaMED mechanisms), Ni and Mn diffusion along the [001] axis. The least squares multiple linear regressions are expressed in the form shown in equation (1), with best fit parameters for each element presented in Supplementary Table 1. Previously the uncertainty structure of diffusion experimental fits has been assumed to be independent causing significant overestimations in uncertainty^{7,12,66}.

$$\ln D_{[001]}^i = a_i + b_i \ln f_{O_2} + c_i X_{Fe} + \frac{q_i + h_i P}{T} + j_i P + k_i \ln a_{SiO_2} \quad (1)$$

P is expressed in Pa, T in K and $\ln f_{O_2}$ in its native form (that is, f_{O_2} is in bar). $D_{[001]}^i$ is the diffusion coefficient parallel to the [001] axis; a_i , b_i , c_i , q_i , h_i , j_i and k_i are the best fit parameters for diffusing species i derived from the multivariate linear regressions. Diffusive anisotropy is taken to be six times faster along the [001] axis than the [010] and [100] axes for each element⁶⁷.

We present the covariance matrices (Supplementary Tables 2 and 3) associated with these new regressions so that the uncertainty structure associated with the experimental fits can be rigorously explored. It is currently accepted that Mn tracer diffusion occurs by a similar mechanism to that of Fe–Mg exchange⁶⁷. Consequently, Fe–Mg diffusion experimental data were used to supplement Mn data to determine the diffusive dependence of Mn on forsterite content. The regressions recover all of the experimental data within 0.5 log₁₀ units and are consistent with previously reported equations^{33,67,68} (Supplementary Fig. 1). Minor differences between the regressions of this study and previous equations (for example Dohmen and Chakraborty³³) are due to slight differences in calibrant datasets. Dohmen and Chakraborty³³ include unpublished diffusion experiments by Meißner⁶⁹, whilst we include more recent data from Spandler and O'Neill²⁴. These differences only culminate in a factor of two difference in recovered timescales for the TaMED Fe–Mg diffusion mechanism, which is minor in comparison to the uncertainties introduced by other parameters (most notably temperature). Recently, a_{SiO_2} was shown to have an influence on the diffusivity of trace elements in olivine (particularly Ni and Mn)^{35,36}; its effect on Fe–Mg has yet to be fully explored due to difficulties in buffering a_{SiO_2} during an exchange reaction³⁰. As previous experiments were not explicitly buffered for a_{SiO_2} , the new data could not be incorporated into the dataset used in the regressions. Separate regressions and covariance matrices for diffusion along [001] were derived for experimental datasets that were explicitly buffered for a_{SiO_2} .

One-dimensional finite element diffusion models developed using FEniCS²⁶ for Fe–Mg exchange, Ni and Mn were combined with a Bayesian inversion, using the MultiNest algorithm^{27,70} and the Python wrapper PyMultiNest⁷¹, to invert for magmatic transport timescales and rigorously assess the associated uncertainties. Each diffusion model used a Crank–Nicholson time-stepping scheme⁷² and linear finite elements were used to represent elemental concentrations. The standard number of mesh points for a profile of length L was set to 300. The number of timesteps in each Monte Carlo realization was kept constant at 300, the sizes of the timestep were therefore not kept constant. During each realization the numerical stability of the solution was assessed using the Courant–Friedrichs–Lewy condition (equation (2)). If the Courant–Friedrichs–Lewy value exceeded 0.5, the mesh was coarsened so that this criteria could be met. However, optimal standard timesteps and mesh intervals were selected initially on the basis of the expected diffusivities and observed lengthscales of diffusion. Therefore any significant mesh coarsening would only occur at conditions far outside the prior values used in the Bayesian inversion. As the diffusivity of all the elements of interest is dependent on forsterite content (equation (1)), a spatially dependent version of Fick's Second Law was used in the modelling (equation (3)). Fe–Mg exchange was treated as nonlinear and was solved first at each timestep using a Newton solver. Ni and Mn diffusion was treated as a linear problem and was solved at each timestep using the corresponding Fe–Mg (forsterite) solution. The models assumed that there was a semi-infinite reservoir that the elements of interest could diffuse into. Dirichlet

boundary conditions (fixed boundary conditions) were therefore maintained at the crystal edge ($x = 0$) and Neumann boundary conditions (no-flux boundary conditions) employed in the crystal interiors ($x = L$). Both Al-based initial conditions (growth and diffusion) and constant initial conditions (diffusion only) were used in the modelling.

$$\frac{\Delta t D}{(\Delta x)^2} < 0.5 \quad (2)$$

in which Δt is the timestep, Δx is the mesh spacing, D is the diffusion coefficient,

$$\frac{\partial C}{\partial t} = \frac{\partial}{\partial x} \left(D(C) \frac{\partial C}{\partial x} \right) \quad (3)$$

in which t is time, x is distance and C is the concentration of the diffusing species.

Boundary conditions: $C = C_0$ on $x = 0$, $\frac{\partial C}{\partial x} = 0$ on $x = L$

In each model, diffusivity parallel to the measured profile (D_p), which accounts for diffusive anisotropy, was calculated using equation (4)^{37,68}:

$$D_p = D_{[100]}\cos^2\alpha + D_{[010]}\cos^2\beta + D_{[001]}\cos^2\gamma \quad (4)$$

in which α , β and γ are the angles between the profile and the [100], [010] and [001] axes respectively. $D_{[100]}$, $D_{[010]}$ and $D_{[001]}$ are the diffusion coefficients parallel to the [100], [010] and [001] axes.

As f_{O_2} was above 10^{-10} Pa, the TaMED diffusion mechanism equation was used for Fe–Mg exchange. A log uniform prior was used for time (0–1,000 d). Independent Gaussian priors, set with 1σ uncertainties, were used for intensive parameters including T , P , $\text{Fe}^{3+}/\text{Fe}_{\text{total}}$ and a_{SiO_2} . Multivariate Gaussian priors were used for coefficients in the diffusion equations, which are controlled by their respective covariance matrices. The variation in T , P and $\text{Fe}^{3+}/\text{Fe}_{\text{total}}$ for each of the runs is also shown in Supplementary Figs. 24–26 with marginal plots shown in Supplementary Figs. 27–46. The log likelihood function of the inversion employed a χ^2 misfit between the model and all measured observations, which were weighted by their analytical uncertainties. The MultiNest algorithm employed ellipsoidal nested sampling^{27,70,71}. A fixed size of parameter vectors or ‘livepoints’ ($n = 400$) were drawn randomly from the prior distributions and were clustered into multidimensional ellipses. New points were selected from the prior within this ellipsoid until one with a likelihood that was greater than the lowest likelihood point was obtained; this point was then removed^{27,70,71}. The selection of diffusion coefficient prior points using the derived covariance matrices reduced the size of the parameter space explored and thus reduced uncertainty. The algorithm terminated once convergence of the marginal likelihood was attained.

In the case of growth-dominated profiles, the inversion timescales were probably the result of smoothing of the Al-based initial conditions, but still demonstrate that there was insufficient time for effective diffusive decoupling within the resolution of conventional olivine geospeedometers (Fe–Mg, Ni, Mn) applied to profiles measured using standard EPMA means⁵².

To assess the effect of a_{SiO_2} , we also modelled the diffusion of Ni and Mn using an a_{SiO_2} for Borgarhraun of approximately 0.62 ± 0.03 and using the a_{SiO_2} -dependent diffusivities^{35,36}. These calculations show that a_{SiO_2} affects the timescale estimates only marginally for Al-based initial conditions: a global median of 12.7 d and 95% quantile of 38.7 d.

Physical modelling. The buoyancy-driven transcrustal magma ascent rate is calculated, which provides a theoretical minimum transport time based on the magma’s physical properties. We assumed laminar flow in the centre of an elliptical dyke, meaning that maximum velocities were calculated. We initially assumed that dyke half-width was approximately 0.5 m, consistent with typical dyke widths of 0.1–7 m observed in Iceland^{40,73}. The mean speed of magma, \bar{u} , through the cross-section of the dyke was calculated using an approximation (equation (5)):

$$\bar{u} \approx \frac{w^2}{12\mu} \Delta\rho g \quad (5)$$

where $\Delta\rho$ is the density difference between the magma and the host rock, w is the dyke half-width, g is gravitational acceleration and μ is the magma viscosity. The host rock density was assumed to be constant at $3,000 \text{ kg m}^{-3}$ throughout the entire crustal column. The melt density was calculated to be $2,820 \text{ kg m}^{-3}$ using the model of Lange and Carmichael⁷⁴ and the intensive parameters and melt composition used in the diffusion modelling (see above). As volatile exsolution has been shown to take place in the shallow crust (CO_2 at approximately 3 km depth and H_2O at approximately 1 km), any density changes associated with exsolution and bubble growth were not considered. Melt viscosity was calculated to be 9 Pa s using the viscosity model of Giordano et al.⁷⁵. The crystal content of Borgarhraun is typically low (8–10%), so any changes in effective viscosity associated with crystallinity were not considered any further. We then rearranged equation (5) to calculate the dyke half-widths that would be required to satisfy thermal and diffusion chronometry constraints.

CO_2 flux estimate calculations. The eruptive volume of Borgarhraun has been estimated as 0.35 km^3 (ref. 17), which is similar to recent large fissure eruptions in

Iceland (such as Holuhraun). The eruption duration and decay in mass eruption rate were therefore assumed to be similar to that measured at Holuhraun³⁸. A similar style of exponential decay in mass eruption rate has been suggested for Laki⁷⁶. The initial mass eruption rate was calculated by integrating the mass eruption curve (equations (6)–(8)) and substituting values for the total mass erupted ($1.015 \times 10^{12} \text{ kg}$, assuming a lava density of $2,900 \text{ kg m}^{-3}$), the eruption duration (6 months) and the decay rate ($1.37 \times 10^{-7} \text{ s}^{-1}$)³⁸.

$$F = F_0 e^{-\lambda t} \quad (6)$$

$$\int_0^{t_e} F dt = M \quad (7)$$

$$F_0 = \frac{M\lambda}{1 - \exp(-\lambda t_e)} \quad (8)$$

in which F is the mass eruption rate, F_0 is the initial mass eruption rate, M is the total mass erupted, t_e is eruption duration, t is time and λ is the decay constant. A bulk melt CO_2 content of 628 ppm was calculated using the average CO_2/Nb content measured in olivine-hosted melt inclusions (391)³⁸ and multiplying it by the measured Nb content of crystal-poor whole rock samples (1.62 ppm)¹⁷. The CO_2 solubility in the melt was then calculated using the parameterization of Shiskina et al.⁴⁹ using Borgarhraun carrier liquid parameters. Exsolution of CO_2 was estimated to start at approximately 3 km depth and was assumed to instantly segregate from the melt (open-system degassing). At such shallow depths the solubility curve becomes almost linear, allowing the rate of CO_2 release from the melt to be assumed to be constant. The rate of CO_2 release was then used in a normalized top hat filter function (s , equation (9)), which was then convolved with the mass eruption curve (equation (10)). The peak in CO_2 flux corresponds to the start of the eruption, where mass eruption rate is at its greatest, and any CO_2 flux before this point was considered to be pre-eruptive for an open-system degassing scenario.

$$s(t) = \begin{cases} 0, & \text{if } 0 < t < \frac{z_{\text{sat}}}{v_z} \\ \frac{dC_{\text{CO}_2}}{dz} v_z, & \text{otherwise} \end{cases} \quad (9)$$

$$f_{\text{CO}_2}(t) = (F * s)(t) \equiv \int_0^t F(\tau) s(t - \tau) d\tau \quad (10)$$

in which f_{CO_2} is the CO_2 flux, v_z is ascent velocity, C_{CO_2} is the concentration of CO_2 , s is the top hat filter, t and τ are time, z is depth and z_{sat} is the depth at which CO_2 becomes saturated in a fluid phase.

Data availability

The data that support the findings of this study, including Supplementary Datasets 1–3 and Excel spreadsheet versions of Supplementary Tables 1–5, are available from the BGS National Geoscience Data Centre at: <https://doi.org/10.5285/0ad0959d-aa0e-4b79-9077-20216a02922a>.

Code availability

We are unable to make the computer code associated with this paper available at this time because it will be the focus of a future methods paper. The diffusion model code and Bayesian inversion in its current format are available on request from the corresponding author.

References

- Bradshaw, R. W. & Kent, A. J. The analytical limits of modeling short diffusion timescales. *Chem. Geol.* **466**, 667–677 (2017).
- QUANTAX CrystalAlign (Bruker Nano, 2010).
- Bachmann, F., Hielscher, R. & Schaefer, H. in *Texture and Anisotropy of Polycrystals III*. vol. 160 (eds Klein, H. & Schwarzer, R. A.) 63–68 (Trans Tech, 2010).
- MATLAB v.9.10.0 (R2016b edition) (MathWorks Inc., 2016).
- Coogan, L., Hain, A., Stahl, S. & Chakraborty, S. Experimental determination of the diffusion coefficient for calcium in olivine between 900 °C and 1500 °C. *Geochim. Cosmochim. Acta* **69**, 3683–3694 (2005).
- Ito, M. & Ganguly, J. Diffusion kinetics of Cr in olivine and ^{53}Mn – ^{53}Cr thermochronology of early solar system objects. *Geochim. Cosmochim. Acta* **70**, 799–809 (2006).
- Oeser, M., Ruprecht, P. & Weyer, S. Combined Fe–Mg chemical and isotopic zoning in olivine constraining magma mixing-to-eruption timescales for the continental arc volcano Irazú (Costa Rica) and Cr diffusion in olivine. *Am. Mineral.* **103**, 582–599 (2018).

59. Jollands, M. et al. Substitution and diffusion of Cr^{2+} and Cr^{3+} in synthetic forsterite and natural olivine at 1200–1500 °C and 1 bar. *Geochim. Cosmochim. Acta* **220**, 407–428 (2018).
60. Costa, F., Dohmen, R. & Chakraborty, S. Time scales of magmatic processes from modeling the zoning patterns of crystals. *Rev. Mineral. Geochem.* **69**, 545–594 (2008).
61. Yang, H.-J., Kinzler, R. J. & Grove, T. Experiments and models of anhydrous, basaltic olivine-plagioclase-augite saturated melts from 0.001 to 10 kbar. *Contrib. Mineral. Petrol.* **124**, 1–18 (1996).
62. Kress, V. C. & Carmichael, I. S. The compressibility of silicate liquids containing Fe_2O_3 and the effect of composition, temperature, oxygen fugacity and pressure on their redox states. *Contrib. Mineral. Petrol.* **108**, 82–92 (1991).
63. Ghiorso, M. S. & Sack, R. O. Chemical mass transfer in magmatic processes IV. A revised and internally consistent thermodynamic model for the interpolation and extrapolation of liquid-solid equilibria in magmatic systems at elevated temperatures and pressures. *Contrib. Mineral. Petrol.* **119**, 197–212 (1995).
64. Gualda, G. A., Ghiorso, M. S., Lemons, R. V. & Carley, T. L. Rhyolite-MELTS: a modified calibration of melts optimized for silica-rich, fluid-bearing magmatic systems. *J. Petrol.* **53**, 875–890 (2012).
65. Sigurdsson, I. A., Steinthorsson, S. & Grönvold, K. Calcium-rich melt inclusions in Cr-spinels from Borgarhraun, northern Iceland. *Earth Planet. Sci. Lett.* **183**, 15–26 (2000).
66. Girona, T. & Costa, F. DIPRA: a user-friendly program to model multi-element diffusion in olivine with applications to timescales of magmatic processes. *Geochem. Geophys. Geosyst.* **14**, 422–431 (2013).
67. Chakraborty, S. Diffusion coefficients in olivine, wadsleyite and ringwoodite. *Rev. Mineral. Geochem.* **72**, 603–639 (2010).
68. Costa, F. & Morgan, D. in *Timescales of Magmatic Processes: From Core to Atmosphere* (eds Dosseto, A. et al.) 125–159 (Blackwell, 2010).
69. Meißner, E. *Messung von kurzen Konzentrationsprofilen mit Hilfe der Analytischen Transmissionselektronenmikroskopie (TEM-EDX) am Beispiel der Bestimmung von Diffusionskoeffizienten für die Mg-Fe-Interdiffusion in Olivin*. PhD thesis, Univ. Bayreuth (2000).
70. Feroz, F., Hobson, M., Cameron, E. & Pettitt, A. Importance nested sampling and the MultiNest algorithm. Preprint at <https://arxiv.org/abs/1306.2144> (2013).
71. Buchner, J. et al. X-ray spectral modelling of the AGN obscuring region in the CDFS: Bayesian model selection and catalogue. *Astron. Astrophys.* **564**, A125 (2014).
72. Crank, J. *The Mathematics of Diffusion* (Oxford Univ. Press, 1979).
73. Paquet, F., Dauteuil, O., Hallot, E. & Moreau, F. Tectonics and magma dynamics coupling in a dyke swarm of Iceland. *J. Struct. Geol.* **29**, 1477–1493 (2007).
74. Lange, R. & Carmichael, I. S. Thermodynamic properties of silicate liquids with emphasis on density, thermal expansion and compressibility. *Rev. Mineral. Geochem.* **24**, 25–64 (1990).
75. Giordano, D., Russell, J. K. & Dingwell, D. B. Viscosity of magmatic liquids: a model. *Earth Planet. Sci. Lett.* **271**, 123–134 (2008).
76. Thordarson, T. & Self, S. The Laki (Skaftár Fires) and Grmsvötn eruptions in 1783–1785. *Bull. Volcanol.* **55**, 233–263 (1993).